Climate Dynamics (2023) 61:4359–4375
https://doi.org/10.1007/s00382-023-06809-4

Effects of large-scale constraint and constraint variables on the high-frequency assimilation of radar reflectivity data in convective precipitation forecasting

Hong Li[1,2] · Jian Sun[3] · Yi Yang[1] · Xiangwei Kong[4] · Ruhui Gan[1]

Received: 23 October 2022 / Accepted: 25 April 2023 / Published online: 6 May 2023

Abstract

High-frequency cyclical assimilation of the retrieved rainwater and estimated in-cloud water vapor by radar reflectivity has positive impacts on convective precipitation forecasting but usually causes overestimation. The application of large-scale constraints will produce more balanced dynamical and thermal fields, which can address the above issue to some degree. In this study, the European Centre for Medium-Range Weather Forecasts (ECMWF) global forecast fields are utilized as large-scale constraints that are imposed on the regional model by the grid nudging method. Two heavy rainfall events that occurred in Jiangsu (the South case) and Hebei (the North case) Provinces with different water vapor background conditions are chosen. The results show that the experiment with dynamical constraints (nudging of the horizontal wind field only) performs the best 6-h precipitation location and intensity forecasts for both cases. The experiment that nudged the water vapor mixing ratio together with the horizontal wind field could significantly weaken the forecast precipitation intensity. Although it produces good precipitation forecasts in the first 3-h for the South case (under higher water vapor conditions), it produces an unreliable precipitation forecast with rapid decay for the North case. For the North case which is accompanied by significant cooling, the experiment nudging the water vapor mixing ratio, temperature and horizontal wind fields simultaneously performs better than the experiment nudging the water vapor mixing ratio together with the horizontal wind field.

Keywords Radar reflectivity · High-frequency assimilation · Large-scale constraint · Grid nudging · Nudging variables

1 Introduction

Assimilation of high temporal (~6 min) and spatial (~250 m) resolution radar data can not only add more small- and medium-scale information for the model's initial field but also can effectively weaken the model's inherent "spin-up" problem (Sun et al. 2014; Clark et al. 2016; Bannister et al. 2020) and thus is vital to improve strong convective weather forecasting (Albers et al. 1996; Gao et al. 2004; Hu et al. 2006a, b; Sokol and Zacharov 2012; Maiello et al. 2014). Radar data can be assimilated by cloud analysis (Albers et al. 1996; Hu et al. 2006a), latent heat nudging (Jones and MacPherson 1997; Sun et al. 2014), ensemble Kalman filtering (Snyder and Zhang 2003; Aksoy et al. 2009, 2010; Dowell et al. 2011; Snook et al. 2015; Zeng et al. 2021), variational data assimilation (Sun and Crook 1997, 1998; Gao et al. 1999; Hu and Xue 2007; Xiao et al. 2009; Wang et al. 2013) and hybrid variational and ensemble methods (Li et al. 2012; Shen et al. 2016). Because the three-dimensional variational (hereafter 3D-Var) method requires less computational cost, the assimilation of radar data based on 3D-Var has long been applied in operational convective forecasting.

As one main detected variable, radar reflectivity can retrieve water vapor and hydrometeors, and its assimilation can effectively adjust the hydrometeor, water vapor, and thermal field information in the initial field of the model

✉ Yi Yang
yangyi@lzu.edu.cn

1 Key Laboratory of Climate Resource Development and Disaster Prevention in Gansu Province, College of Atmospheric Sciences, Lanzhou University, Lanzhou 730000, China

2 Institute of Arid Meteorology, China Meteorological Administration, Lanzhou 730020, China

3 China Meteorological Administration Earth System Modeling and Prediction Centre, Beijing 100081, China

4 Lanzhou Central Meteorological Observatory, Lanzhou 730020, China

(Albers et al. 1996; Sun and Crook 1997, 1998; Hu et al. 2006a; Zhao and Xue 2009; Zhao et al. 2012; Wang et al. 2013; Lai et al. 2019). One of the problems currently faced is that the observational information added by radar reflectivity tends to disappear quickly (Aksoy et al. 2010; Mandapaka et al. 2012; Supinie et al. 2017), and high-frequency (a few to dozens of minutes) cyclic assimilation is a feasible way to remedy this and has been proven to produce more accurate forecasts (Hu and Xue 2007; Dong and Xue 2013; Pan and Wang 2019; Hu et al. 2021). However, the rapid cyclical assimilation of radar reflectivity data is more likely to produce spurious or overestimated precipitation (Vendrasco et al. 2016; Gao et al. 2018) in the first few forecast hours caused by an initial imbalance, i.e., the “spin-down” problem (Schwartz and Liu 2014). Some studies have been performed to address this issue, among which one type considers assimilating the real nonconvective information. For example, Gao et al. (2018) assimilated "nonprecipitation echo" (S-band less than 10 dBZ) to reduce the excess water vapor information, and similar works have been performed by Aksoy et al. (2009) and Tong and Xue (2005). In addition, Gan et al. (2022) assimilated the “zero” column maximum vertical velocity, i.e., the average maximum vertical velocity over the no-rain echo region in the background field, to suppress spurious convection. This kind of method is effective, but more observation information is needed.

Another promising method is the application of large-scale constraints from the perspective of scale analysis. Radar observations represent convective-scale phenomena, and multiple assimilations of such data will cause the final analysis field to deviate from the large-scale pattern. The large-scale constraint method aims to maintain a large-scale balance by assimilating (Vendrasco et al. 2016; Tang et al. 2019; Wang et al. 2021) or nudging (Yue et al. 2018; Lin et al. 2021) a large-scale analysis in a rapidly updated 3D-Var radar assimilation system. For example, Vendrasco et al. (2016) assimilated a large-scale analysis [from the National Center for Environmental Prediction (NCEP) Global Forecast System (GFS)] at analysis times using the 3D-Var method. Lin et al. (2021) imposed a large-scale constraint (from the NCEP GFS data) on the model forecast periods using the spectral nudging technique to improve short-term quantitative precipitation forecasts of a summer convective case that occurred in southeast China. As the global forecast data issued by ECMWF perform well (Gong et al. 2015; Ran et al. 2018; Liu et al. 2021), it is worth believing that it can provide accurate large-scale information. However, to the best of our knowledge, the ECMWF global forecasts employed as large-scale constraints have not been assessed. In addition, the variables assimilated or nudged include the horizontal wind components, temperature, relative humidity (Wang et al. 2021), water vapor mixing ratio (Vendrasco et al. 2016; Tang et al. 2019), and geopotential height (Yue et al. 2018; Lin et al. 2021) fields, which are constrained simultaneously in the mentioned studies, and the effect of different variables as constraints needs further discussion. Therefore, this study aims to evaluate the effect of the ECMWF global forecast fields employed as large-scale constraints during the simulation periods in a rapidly updated 3D-Var radar assimilation system. The effect of the different variables as constraints will be discussed. Grid nudging is used to achieve the constraints because the minimum wavenumbers needed by spectral nudging are sometimes not easy to control for a regional (limited area) model forecast.

The amount and length of precipitation in eastern China are closely related to the East Asian summer monsoon, which is an important source of water vapor (Tang et al. 2009; Zeng et al. 2016). Considering that the difference in precipitation characteristics caused by different water vapor conditions may be sensitive to constraint variables, two heavy rainfall events that occurred in the East Asian summer monsoon-affected area (the South case under higher water vapor conditions) and the East Asian summer monsoon transition zone (the North case under lower water vapor conditions) are selected to see the results under different water vapor background conditions. Section 2 contains a description of these two cases. The effects of the large-scale constraint based on ECMWF global forecast data and different constraint variables are the focus of this study. The structure of the present study is as follows: Sect. 2 describes observations and the methodology, including the forecast model used, i.e., WRF, and its 3D-Var system. In addition, the radar reflectivity assimilation scheme and the grid nudging method used by the large-scale constraint are briefly introduced. The experimental settings are presented in Sect. 3. Section 4 gives the experimental results, and the last section is devoted to the conclusion.

2 Data and methods

Two heavy rainfall events occurred in Jiangsu Province on 6 July 2019 (hereafter the South case) and in Hebei Province on 4 July 2020 (hereafter the North case) are chosen. From the precipitation observations (an hourly precipitation grid dataset created by merging data from China automatic stations with Climate Prediction Center (CPC) morphing technique (CMORPH) precipitation products), the main precipitation period for the South case is from 0700 to 1300 UTC, 6 July 2019. The maximum 6-h accumulated precipitation is over 74 mm, with the hourly accumulated precipitation reaching up to 63 mm. The 500 hPa circulation pattern and the wind field and water vapor configuration at 850 hPa (from the ECMWF Reanalysis 5, i.e., ERA5 hourly data) at 0600 UTC, 6 July 2019 for the South

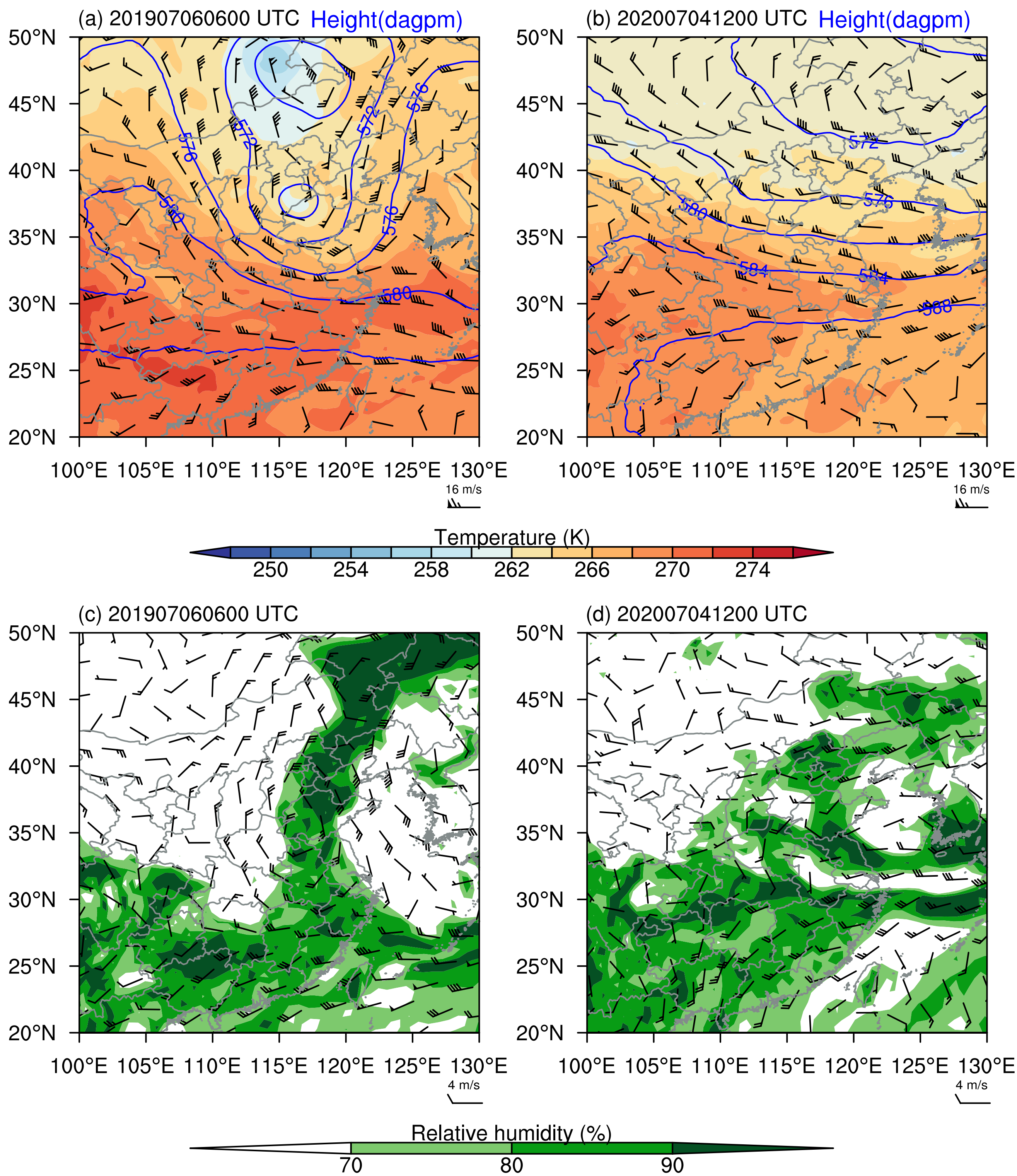

Fig. 1 The wind, temperature, and geopotential height fields at 500 hPa (**a**) and the wind and relative humidity fields at 850 hPa (**c**) from ERA5 for the South case at 0600 UTC on 6 July 2019. **b**, **d** Are the same as **a** and **c** but are for the North case at 1200 UTC on 4 July 2020

case are shown in Fig. 1a, c. Jiangsu Province is located at the southern boundary of the cold-low vortex, and it is dominated by cold advection at 500 hPa. At 850 hPa, the northerly and southerly winds with equivalent strength converge and thus form a wind shear line along the Hebei, Shandong, and Jiangsu Provinces. Such a configuration at high and low altitudes increases the instability of the air column and enables heavy rainfall locally in the short term. For the North case, precipitation in Hebei Province mainly occurred from 1300 to 2100 UTC on 4 July 2020. The maximum 8-h accumulated precipitation is over 77 mm, with the hourly accumulated precipitation reaching up to 42 mm. From the 500 hPa circulation at 1200 UTC on 4 July 2020 (Fig. 1b), the transit of the cold trough delivers dry and cold air from high latitudes to Hebei Province, while a weak wind shear accompanied by the southwest warm and humid airflow exists at 850 hPa (Fig. 1d).

2.1 Doppler radar data and the ECMWF global forecast data

The radar observations are provided by the CINRAD WSR-98D weather radars. For the South case, reflectivity observations from a total of eight Doppler radars (Fig. 2a) located in Linyi, Ji'nan, Qingdao, Puyang, Lianyungang, Xuzhou, Huai'an, and Bengbu cities are used. Seven Doppler radars (Fig. 2b) located in Chengde, Qinghuangdao, Beijing, Tanggu, Shijiazhuang, Cangzhou, and Handan cities are used for the North case. All of the radars mentioned above are S-bands with a maximum range of 230 km except the one located in Chengde, which is a C-band with a maximum range of 200 km. The radars perform a volume scan every 5–6 min at 9 elevation angles, including 0.5°, 1.5°, 2.4°, 3.4°, 4.3°, 6.0°, 9.9°, 14.6°, and 19.5°. Raw radar reflectivity observations have a resolution of 1 km; they are first processed by a quality control (e.g., the removal of clutter) procedure, interpolated to the model's grids and then used for assimilation.

The ECMWF global forecast data used as large-scale constraints provide forecasts with a time interval of 3 h. The forecast variables include the horizontal wind components u, v, vertical velocity w, temperature T, relative humidity rh, and other variables at 19 pressure levels (10–1000 hPa) with a horizontal resolution of $0.25° \times 0.25°$.

2.2 WRF 3D-Var system and grid nudging method

In this study, the Weather Research and Forecasting (WRF) model, version 4.1.2, is used to generate the forecast. The assimilation system used is the WRF 3D-Var data assimilation system, which aims to seek an optimal estimate of the true atmospheric state by combining observations and background forecasts. The best analysis is defined by minimizing a cost function J:

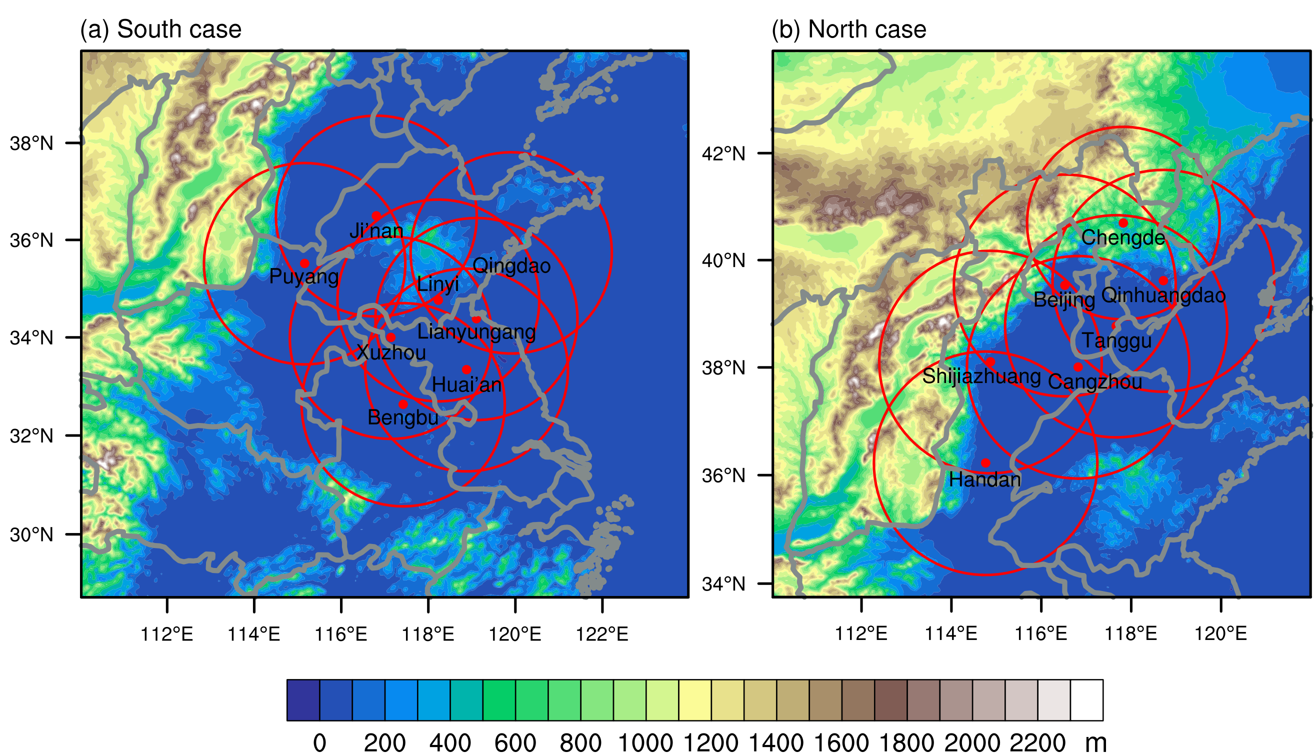

Fig. 2 Terrain heights (shaded; m) and locations (solid red dots) of the 8 radars used for the South case (**a**) and the 7 radars used for the North case (**b**). The red circles around red dots indicate the maximum available detection ranges for each radar (200 km for the Chengde radar station and 230 km for the other radar stations)

$$J(x) = J^b(x) + J^o(x) = \frac{1}{2}\left(x - x^b\right)^T B^{-1}\left(x - x^b\right) + \frac{1}{2}(H(x) - y^o)^T O^{-1}(H(x) - y^o), \quad (1)$$

where $J^b(x)$ and $J^o(x)$ stand for the background and observation terms, respectively. x is the analysis variable, x^b is the background variable, y^o represents the observations, and O is the observation error covariance matrix. The performance of 3D-Var is greatly dependent on the background error covariance (BE), i.e., the matrix B in Eq. (1). In this study, the BEs for both rainfall cases are obtained using the National Meteorological Center (NMC) method. In Eq. (1), H is the observation operator, for radar reflectivity observations, the indirect assimilation scheme developed by Wang et al. (2013) is used. In addition, the radar reflectivity observations are assimilated with an interval of 20 min.

In this study, the large-scale constraint aims to nudge the model toward the ECMWF global forecast fields by the grid nudging (GN) method. The GN method (Stauffer and Seaman 1990) is an empirically based four-dimensional data assimilation method. The core idea is to add an additional relaxation term to forecast equations. The relaxation term, which is based on the difference between the simulated value and the ECMWF global forecast data, makes the solution of the WRF forecast equation closer to the ECMWF global forecast data. In WRF, the predictive equation of variable $\alpha(x, t)$ mass weighted by pressure p^* is written as:

$$\frac{\partial p^* \alpha}{\partial t} = F(\alpha, x, t) + G_\alpha \times W_\alpha \times \varepsilon_\alpha \times p^*\left(\widehat{\alpha}_0 - \alpha\right), \quad (2)$$

$$p^* = p_s - p_t, \quad (3)$$

where p_t is the pressure at the top of the model, p_s is the surface pressure, x are independent spatial variables, t is time, $F(\alpha, x, t)$ represents the model's physical forcing terms, W_α is a four-dimensional weighting function, ε_α is a factor ranging from 0 to 1, and $\widehat{\alpha}_0$ in this study is the variable of the ECMWF global forecast data for α analyzed to the model grid. The nudging coefficient G_α determines the relative magnitude of the relaxation term ($1/\Delta t$, where Δt is the time scale in seconds). For the GN method, α can be the zonal and meridian wind components (u, v), the temperature (T), and the water vapor mixing ratio (q).

3 Experimental design

Single domains centered at (33.0° N, 117.0° E) and (40.16° N, 114.35° E) with horizontal grid spacing are set as 4 and 3 km, and domain sizes of 401 × 401 and 550 × 424 are used for the South and North cases, respectively. The NCEP GFS data are used to generate the initial and lateral boundary conditions. The domain comprises 50 vertical pressure levels, with the top-level set at 50 hPa. The WSM 6-class microphysics scheme (Hong and Lim 2006), Goddard shortwave scheme (Chou and Suarez 1999), RRTM longwave scheme

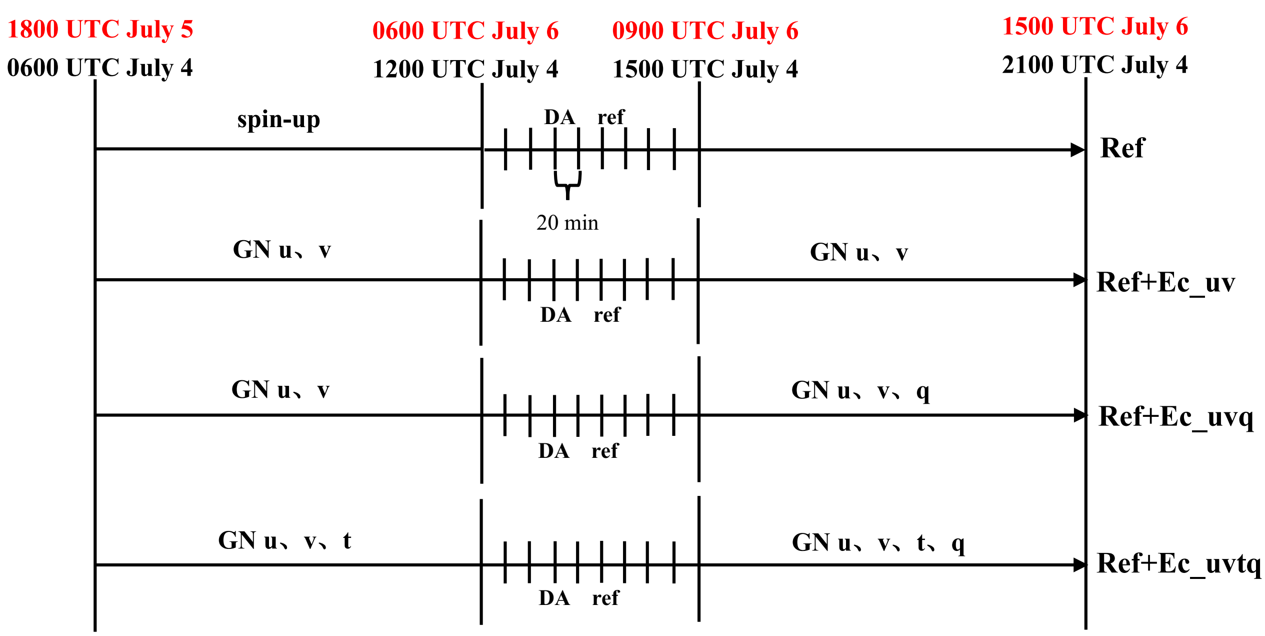

Fig. 3 Scheme of the numerical experiments for the South case (time written in red) and the North case (time written in black). The symbol "DA ref" means assimilating radar reflectivity, and "GN" means nudging by the grid nudging method

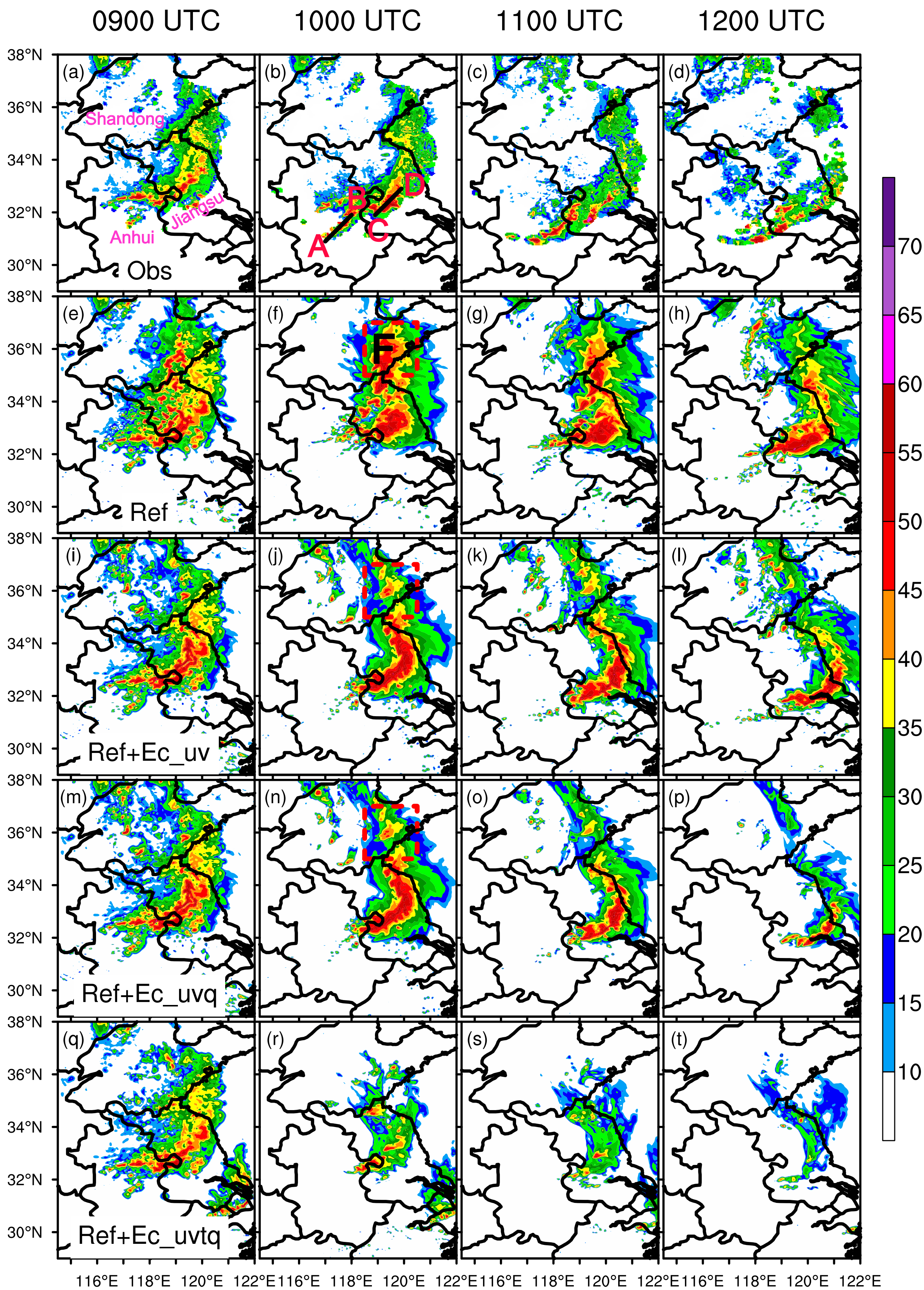
0900 UTC
1000 UTC
1100 UTC
1200 UTC
(a)
(b)
(c)
(d)
Shandong
Jiangsu
Anhui
Obs
A
B
C
D
(e)
(f)
(g)
(h)
F
Ref
(i)
(j)
(k)
(l)
Ref+Ec_uv
(m)
(n)
(o)
(p)
Ref+Ec_uvq
(q)
(r)
(s)
(t)
Ref+Ec_uvtq
38°N
36°N
34°N
32°N
30°N
116°E
118°E
120°E
122°E
10
15
20
25
30
35
40
45
50
55
60
65
70

◂**Fig. 4** The observed (Obs; **a**–**d**) and forecast composite reflectivity (units: dBZ) at the last analysis time (0900 UTC) and different forecast times of the **e**–**h** Ref, **i**–**l** Ref+Ec_uv, **m**–**p** Ref+Ec_uvq, and **q**–**t** Ref+Ec_uvtq experiments for the South case on 6 July 2019. The areas framed by dotted red lines in **f**, **j**, **n** represent the places where spurious strong echoes exist in the Ref experiment

(Mlawer et al. 1997), YSU planetary boundary layer scheme (Hong et al. 2006), and no cumulus parameterization are used.

A brief schematic diagram of the experimental design for two rainfall cases is given in Fig. 3. Taking the North case as an example, all experiments are initialized at 0600 UTC on July 4, 2020, and run for 15 h. A baseline control experiment (the Ref experiment) refers to one in which only radar reflectivity data are cyclically assimilated with an interval of 20 min (refer to Pan and Wang 2019) from 1200 to 1500 UTC. The first 6 h (0600–1200 UTC) of the Ref experiment are considered as the spin-up time. The Ref+Ec_uv experiment uses the same settings as that of the Ref experiment but nudges the u and v fields during 0600–1200 UTC and 1500–2100 UTC. The Ref+Ec_uvq experiment further nudges the q field from 1500 to 2100 UTC. On the basis of the Ref+Ec_uvq experiment, the Ref+Ec_uvtq experiment further nudges the T field during 0600–1200 UTC and 1500–2100 UTC. The reason we nudge the q field only during 1500–2100 UTC is that the wetting of the model's field occurs after the high-frequency cyclical assimilation of radar reflectivity observations. All nudging coefficients used here are 9×10^{-4} (s^{-1}) (approximately a time interval of 3 h).

4 Results

4.1 Constraint evaluation for the South case

First, the effect of the constraint on the analysis and forecast is tested for the South case. The observed composite reflectivity from 0900 to 1200 UTC on 6 July 2019 is shown in Fig. 4a–d, from which we can see that there is a strong echo (> 35 dBZ) belt along central Jiangsu to central and eastern Anhui Province at the last analysis time (0900 UTC). In the subsequent 3 h, such a strong but narrow belt gradually moves southeastward with little change in intensity. For the Ref experiment, the strong echo belt along Jiangsu to Anhui Province is stronger and wider than the observations, and false strong echo areas exist in Shandong Province (area F in Fig. 4f). With the u, v fields nudged, the forecast location of the strong echo zone is significantly improved. Specifically, false echoes in Shandong Province are effectively weakened, and the strong echo belt is narrower and closer to the observations. However, the overall echo strength is also stronger than the observed echo strength. Furthermore, with the q field nudged (the Ref+Ec_uvq experiment) after the last analysis time, this strong echo belt forecast has been further improved with a similar location as that of the Ref+Ec_uv experiment. Although the Ref+Ec_uvq experiment yields an improved forecast, further nudging the T field produces the worst forecast (the forecast reflectivity echoes are much weaker than the observed reflectivity echoes, and false echo forecast exists in the southeast corner of the domain).

From the 3-h forecast for composite reflectivity, the Ref+Ec_uv and Ref+Ec_uvq experiments have better performance than the Ref experiment. How did the forecast improve? Lines A–B and C–D (shown in Fig. 4b) indicate two observed main strong echo belts, which always correspond to strong updraft velocities, strong horizontal wind and water vapor convergences at the near-surface layer. From Fig. 5a–c, the vertical velocity sections along line A–B of the Ref, Ref+Ec_uv, and Ref+Ec_uvq experiments are not significantly different, i.e., the vertical velocity at all layers is relatively small (~ 1 m/s). However, the vertical velocity sections along line C–D (Fig. 5e–g) show that the vertical velocities of the Ref+Ec_uv and Ref+Ec_uvq experiments are obviously stronger (the maximum updraft velocity can reach up to 4 m/s) than those of the Ref experiment (almost 2–3 m/s). Specifically, the vertical velocities of the Ref+Ec_uvq experiment are slightly less than those of the Ref+Ec_uv experiment (Fig. 5h), which contributes to weaker precipitation forecasts than the Ref+Ec_uv experiment. From the geopotential height and wind fields at 500 hPa (Fig. 6a, b), the Ref and Ref+Ec_uvq experiments show a slight difference. Jiangsu Province is located at the lower boundary of the cold-low vortex for both experiments. However, obvious differences exist between the Ref and Ref+Ec_uvq experiment at 850 hPa. Figure 6d–f show the differences in the horizontal wind and relative humidity fields between different experiments and the ERA5 data at 850 hPa. From Fig. 6e, f, the differences between the Ref+Ec_uv experiment and the ERA5 data are similar to the differences between the Ref+Ec_uvq experiment and the ERA5 data, and an extra obvious horizontal wind convergence occurs along the observed location of strong echoes (the brown dotted line in Fig. 6c–f), on the north side of which there is a stronger northerly wind, while there is a stronger southwesterly wind on the south side. This convergence increment at the lower level is conducive to the enhancement of vertical motion. At the same time, one possible reason for the spurious reflectivity forecast (the box in the red dotted line in Fig. 6d) of the Ref experiment (domain F, as shown in Fig. 4f) may be the enhanced southerly wind in this area. This warmer and humid southerly wind transports more water vapor here and increases the instability of the air column, which makes it more likely to cause convection. After nudging the u, v or the u, v, and q fields (Fig. 6e,

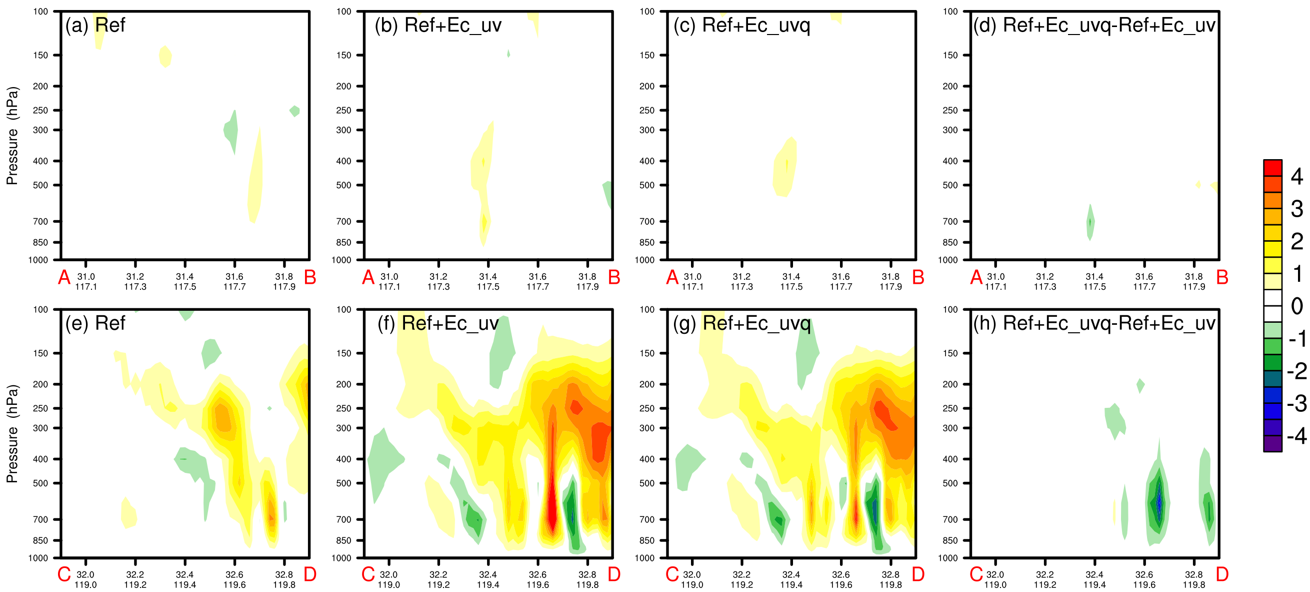

Fig. 5 Cross-sections of the vertical velocity (units: m/s) at 1000 UTC on 6 July 2019 along lines A–B (**a**–**d**) and C–D (**e**–**h**) in Fig. 4b for the Ref (**a**, **e**), Ref+Ec_uv (**b**, **f**), and Ref+Ec_uvq (**c**, **g**) experiments for the South case. **d**, **h** Are the differences between the Ref+Ec_uv and Ref+Ec_uvq experiments

f), this issue is improved with a weakened relative humidity field and a weakened southerly wind.

Figure 7 shows the forecast hourly accumulated precipitation. The Ref experiment can basically capture the main rain belt (along the central and southern Jiangsu Province to southern Anhui Province) with a slight northerly inclination, but it always produces stronger precipitation than the observations. In addition, obvious spurious precipitation exists in Shandong Province (the area framed by the dotted purple line in Fig. 7) in the Ref experiment. Such spurious precipitation can be weakened effectively after nudging the u, v (the Ref+Ec_uv experiment) or the u, v, and q (the Ref+Ec_uvq experiment) fields. Meanwhile, the forecast main rain belts of both experiments are more southerly compared to the Ref experiment, which results in more consistency with the observed rain belt. In terms of rainfall intensity, the Ref+Ec_uvq experiment has better behavior than the Ref+Ec_uv experiment. Similar to the echo forecast, the Ref+Ec_uvtq experiment produces the worst precipitation forecast.

The forecast skills of the hourly accumulated precipitation are shown in Fig. 8. The equitable threat score (ETS; Gandin and Murphy 1992) and the neighborhood-based fractions skill score (FSS; Roberts and Lean 2008) are employed for verification. The better the forecast, the closer the value of ETS or FSS is to 1. Compared to the Ref experiment, the Ref+Ec_uv experiment improves the ETS (FSS) within the 6-h (5-h) forecast for thresholds of 1, 5, and 20 mm/h, which indicates that nudging the u and v fields of the ECMWF global forecast data has a positive effect on the precipitation position forecast. For the South case, the Ref+EC_uvtq experiment obtains the lowest scores.

4.2 Constraint evaluation for the North case

From the above analysis, the Ref+Ec_uv experiment achieves the best 6-h forecast, and the Ref+Ec_uvq experiment behaves better in the first 3-h forecast for the South case. However, the conclusions are different for the North case. From 1500 to 1900 UTC on 4 July 2020, the observed intense reflectivity belt is located in Cangzhou City (the area framed by the dotted purple line in Fig. 9), which is stable slowly moving. With the u, v, and q fields nudged (Fig. 9p–t), the forecast intense reflectivity gradually disappears within the next 4 h after the last analysis time (1500 UTC), which is inconsistent with the observations. Although the Ref+Ec_uvq experiment makes the worst forecast, the Ref+Ec_uv experiment still produces a better forecast than the Ref experiment. The strong echo center in Hebei Province predicted by the Ref experiment is generally too northerly and has a larger coverage compared to observations, and the echo intensity in east of the southern border of Hebei Province is stronger and the coverage is wider. The Ref+Ec_uv experiment produces a more southerly strong echo area, which is closer to the observations. It is worth noting that the Ref+Ec_uvtq experiment produces better results than the Ref+Ec_uvq experiment, and the echo coverage forecast is highly consistent with the observations.

From the vertical cross sections (Fig. 10) through the observed strong echo (line A–B in Fig. 9e) at the

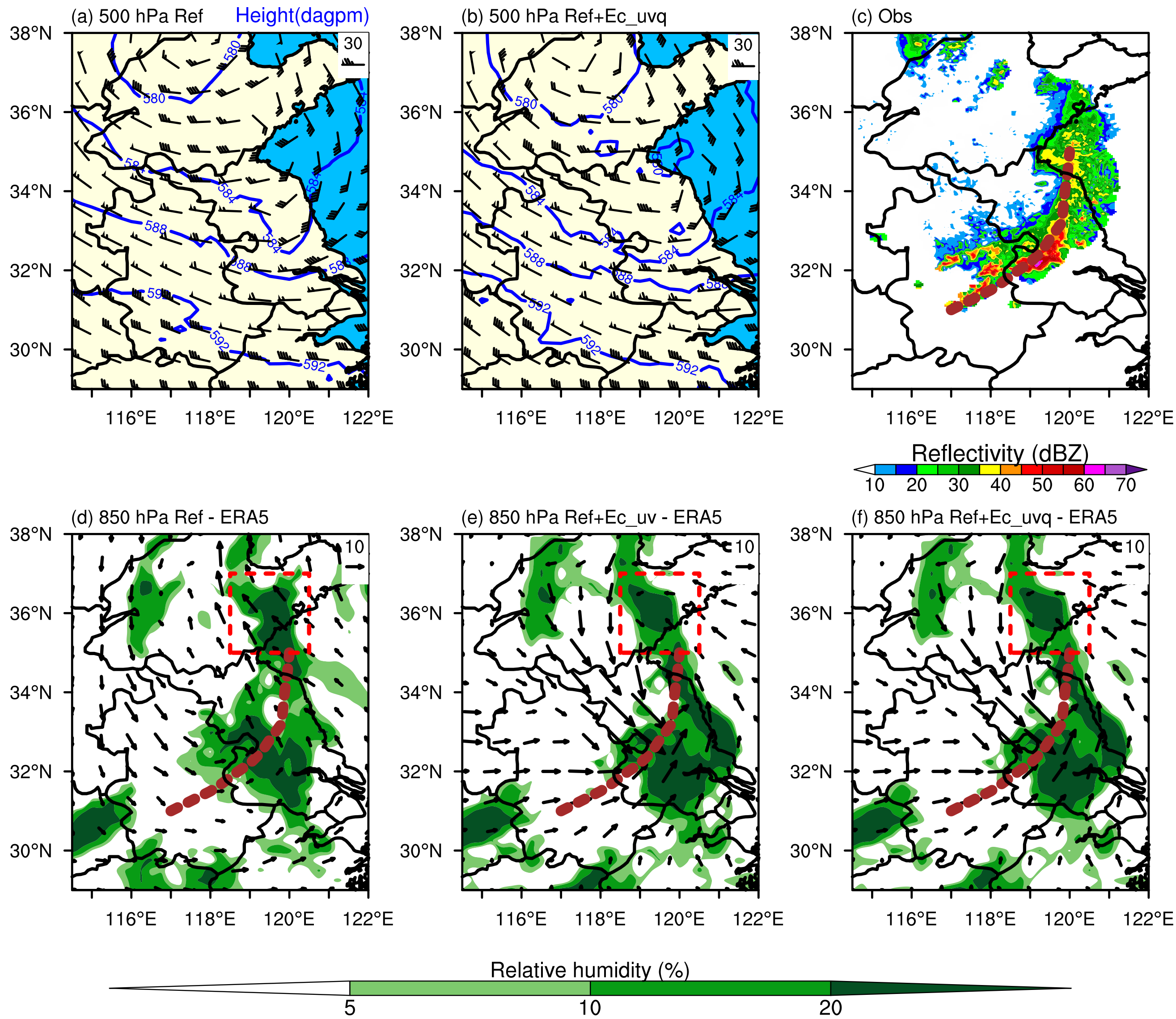

Fig. 6 The wind and geopotential height fields at 500 hPa for the **a** Ref and **b** Ref+Ec_uvq experiments at 1000 UTC on 6 July 2019 for the South case. The simultaneously **c** observed composite reflectivity (units: dBZ) and the wind and relative humidity fields (shaded) difference at 850 hPa between the **d** Ref experiment and ERA5. (**e**, **f**) Is the same as **d** but is the difference between the Ref+Ec_uv (Ref+Ec_uvq) experiment and ERA5. The brown dotted lines in **c**–**f** indicate the observed strong echo belt positions, and the areas framed by red dotted lines represent the places where spurious strong echoes exist in the Ref experiment, as in Fig. 4f, j, n

fourth forecast hour, the strong echo area (> 35 dBZ) of the Ref experiment is in the northern part of the section and reaches ~ 250 hPa in the vertical direction. Accordingly, the Ref experiment also produces certain vertical velocities and snow above 500 hPa in the northern part of the section. With the u and v fields nudged, the strong echo area moves southward and with stronger intensity at lower layers. The area with large vertical velocities also moves southward and is mainly distributed below 400 hPa (Fig. 10f), and the rainwater field below 700 hPa is slightly enhanced. The Ref+Ec_uvq experiment has no vertical velocity or hydrometeors along the section and only maintains weakened water vapor below the middle and lower layers of the model. However, when nudging the u, v, T, and q fields together, the strong echo area has a similar zonal position to that of the Ref+Ec_uv experiment but is mainly concentrated below 400 hPa. The vertical velocity distribution is also similar to the Ref+Ec_uv experiment, but with a stronger upward motion, more rainwater (hail) occurs below (above) 700 hPa but weakens mid- and low-level water vapor and snow.

From the hourly accumulated precipitation (Fig. 11), the forecast precipitation by the Ref experiment is too northerly, and spurious precipitation exists east of southern Hebei

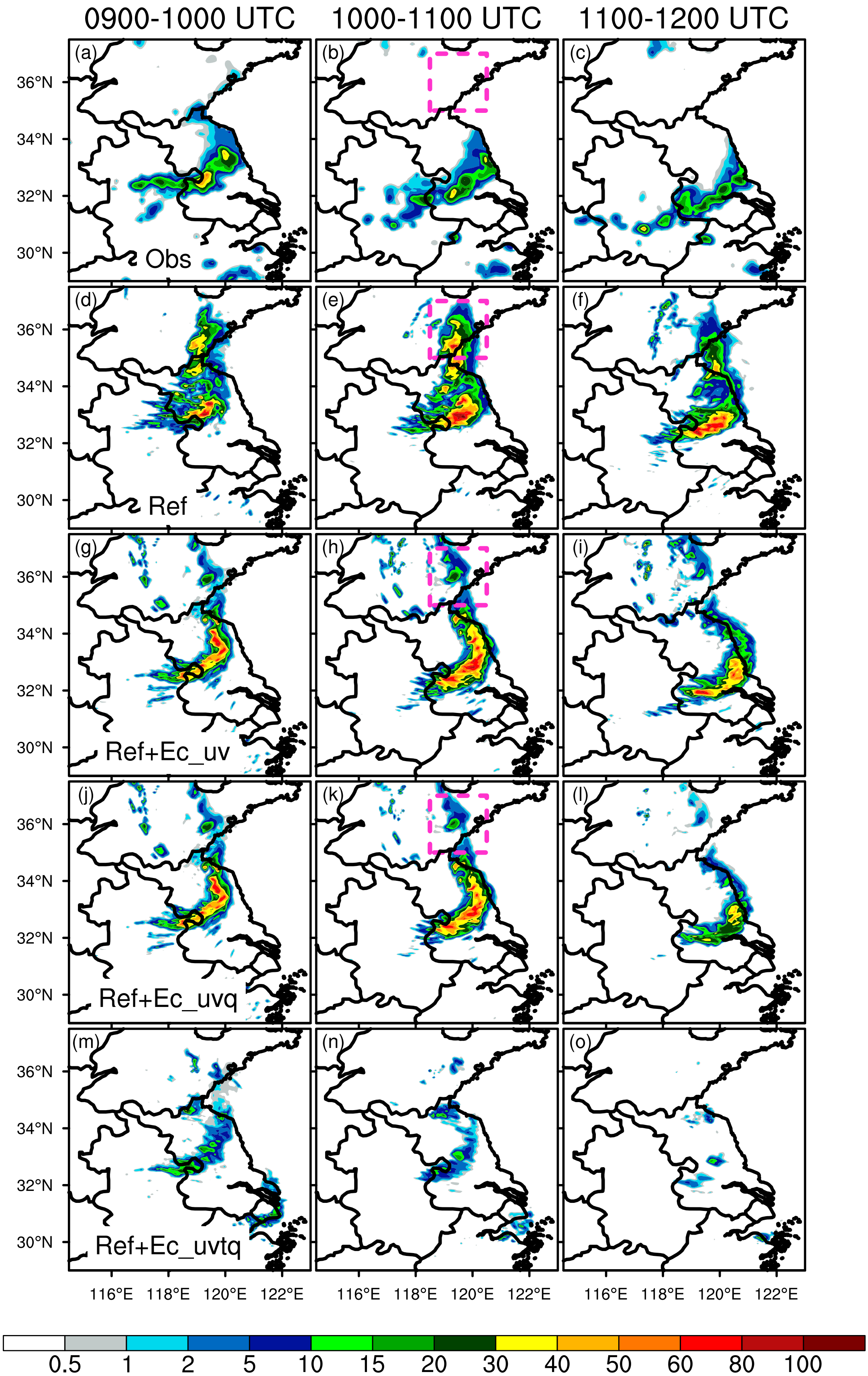
0900-1000 UTC
1000-1100 UTC
1100-1200 UTC
(a)
(b)
(c)
(d)
(e)
(f)
(g)
(h)
(i)
(j)
(k)
(l)
(m)
(n)
(o)
Obs
Ref
Ref+Ec_uv
Ref+Ec_uvq
Ref+Ec_uvtq
36°N
34°N
32°N
30°N
116°E
118°E
120°E
122°E
0.5
1
2
5
10
15
20
30
40
50
60
80
100

◂**Fig. 7** Hourly accumulated precipitation (units: mm) for the South case on 6 July 2019 from **a**–**c** observations (Obs), the **d**–**f** Ref, **g**–**i** Ref+Ec_uv, **j**–**l** Ref+Ec_uvq, and **m**–**o** Ref+Ec_uvtq experiments. The last analysis time of the case is 0900 UTC on 6 July 2019. The areas framed by dotted purple lines in **b**, **e**, **h**, **k** represent the places where spurious strong echoes exist in the Ref experiment

Province. Compared to the Ref and Ref+EC_uvq experiments, the Ref+EC_uv experiment has a better forecast of the main observed precipitation area (the area framed by the dotted purple line) and reduces spurious precipitation. Although spurious precipitation can be further suppressed, the forecast main precipitation area of the Ref+EC_uvtq experiment is slightly westerly compared to the observed area. Compared to the Ref experiment, the Ref+Ec_uv experiment improves the FSS within the 6-h forecast for thresholds of 1, 5, and 20 mm/h (Fig. 12). The Ref+Ec_uvq experiment obtains the lowest scores. The Ref+EC_uvtq experiment obtains the lowest scores for the South case but behaves better than the Ref+EC_uvq experiment for the North case.

4.3 Analysis of the difference between two cases

From the above case studies, nudging the q and T fields of the ECMWF global forecast data produces different effects on the forecast for the two cases chosen. To find the possible reasons, the time evolutions of the averaged q and T values at 850 hPa in specific areas for the two cases are analyzed (Fig. 13) to study the characteristics of the two cases (see the Fig. 13 caption for the specific area boundaries). The statistics are calculated based on the results of the Ref experiments, and the area selected for each case is based on the development of radar echoes. In the area, radar echoes grow from nothing, strengthen gradually, and weaken until they dissipate during the simulation time period. It is found that the averaged value of q of the Ref experiment has a significant decrease (~ 4.5 g/kg; 14.96 g/kg at 0900 UTC to 10.53 g/kg at 1500 UTC on 6 July 2019) but with a slight change in the averaged value of T (18.55 °C at 0900 UTC to 18.25 °C at 1500 UTC on 6 July 2019) during the simulation period for the South case. The result is different for the North case; during the simulation period, the change in the averaged value of q of the Ref experiment (~ 1.2 g/kg; 11.76 g/kg at 1300 UTC to 10.54 g/kg at 2100 UTC on 4 July 2020) is much smaller than that of the South case, while the average temperature decrease is significant (approximately 2.3 °C; 19.42 °C at 1200 UTC to 17.11 °C at 2100 UTC on 4 July 2020). Therefore, in the reference simulation, precipitation is mainly produced by sacrificing water vapor for the South case. For the North case, the cooling condensation caused by cold air transit also plays a considerable role in producing precipitation, although southwesterly water vapor transport existed at 850 hPa.

Compared to the average values of q and T of the ECMWF global forecast data for the South case (blue dots in Fig. 13a, b), the average value of q (T) of the Ref experiment is higher (smaller). Thus, the Ref+EC_uvtq experiment reduces the chance of rainfall by nudging smaller q and higher T of the ECMWF global forecast data. For the North case, although the average value of q of the ECMWF global forecast data is also smaller than that of the Ref experiment, the average value of T of the ECMWF global forecast data is lower than that of the Ref experiment in the first 3-h (1500–1800 UTC in Fig. 13d) forecast. This leads to an increased rainfall chance of the Ref+EC_uvtq experiment compared to that of the Ref+EC_uvq experiment. Different water vapor conditions, precipitation characteristics, and the

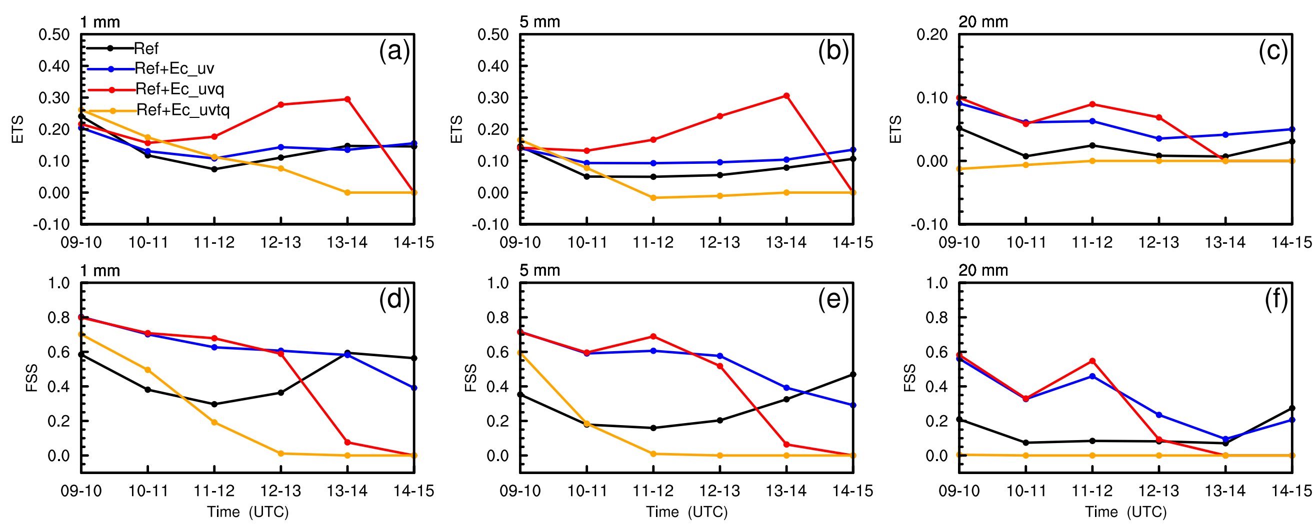

Fig. 8 ETS (**a**–**c**) and FSS (**d**–**e**) of the predicted hourly accumulated precipitation of the Ref, Ref+Ec_uv, Ref+Ec_uvq, and Ref+Ec_uvtq experiments for thresholds of 1, 5, and 20 mm/h for the South case on 6 July 2019

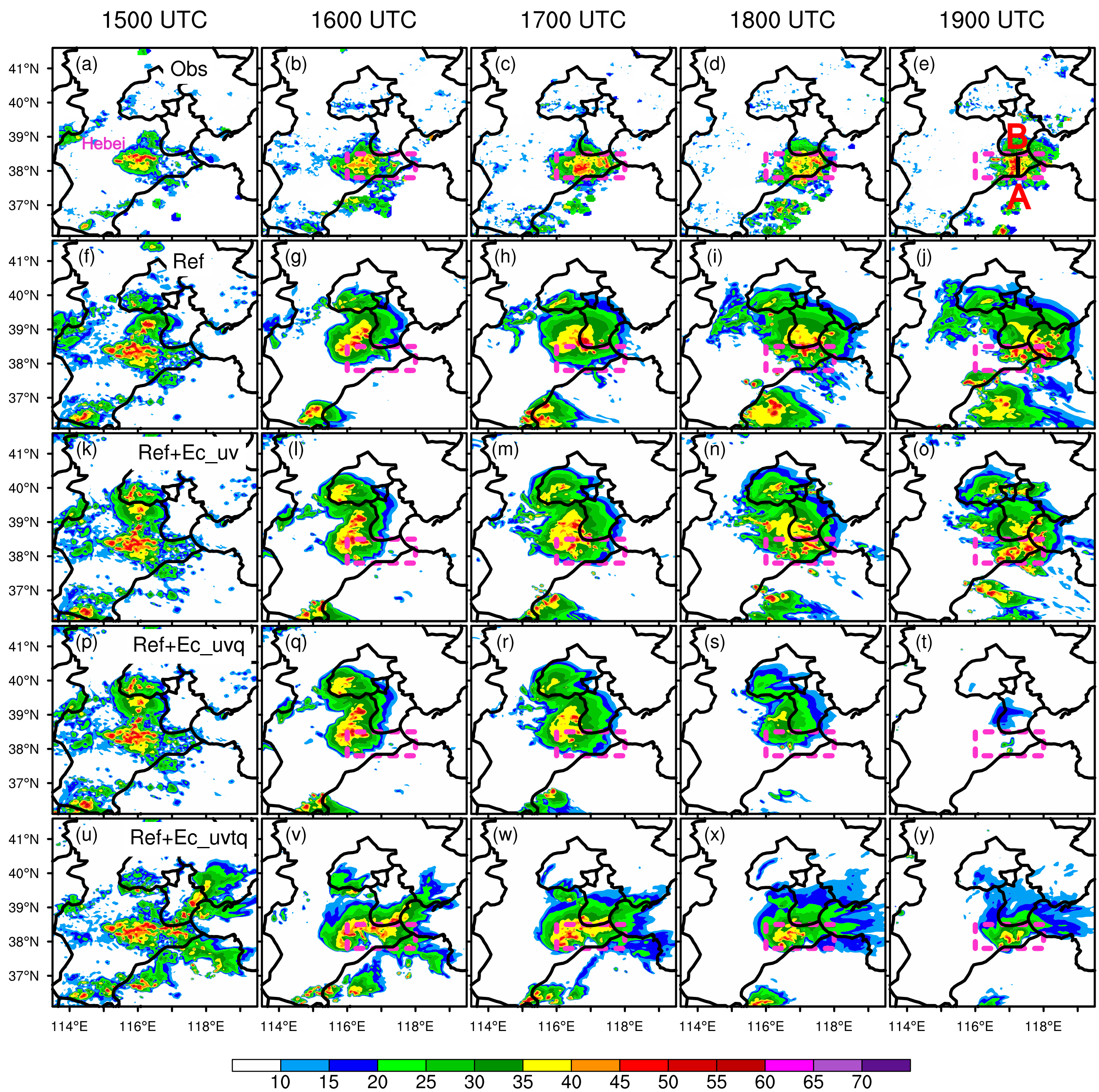

Fig. 9 The observed (**a–e**; Obs) and forecast composite reflectivity (units: dBZ) at the last analysis time (1500 UTC) and different forecast times of the **f–j** Ref, **k–o** Ref+Ec_uv, **p–t** Ref+Ec_uvq, and **u–y** Ref+Ec_uvtq experiments for the North case on 4 July 2020. The areas framed by dotted purple lines in **b–e**, **g–j**, **l–o**, **q–t**, and **v–y** indicate the observed main strong echo zone

difference between the large-scale analysis (the ECMWF global forecast data) and the model may result in different forecast effects of nudging the q or T fields.

5 Summary and discussion

In this study, the ECMWF global forecast data are utilized as large-scale constraints to improve the positional deviation and overestimated intensity of precipitation forecasts caused by the rapid cyclical assimilation of radar reflectivity data. The grid nudging method is employed to achieve the constraint by forcing the model fields to be close to the u, v, T, and q fields of the ECMWF global forecast data.

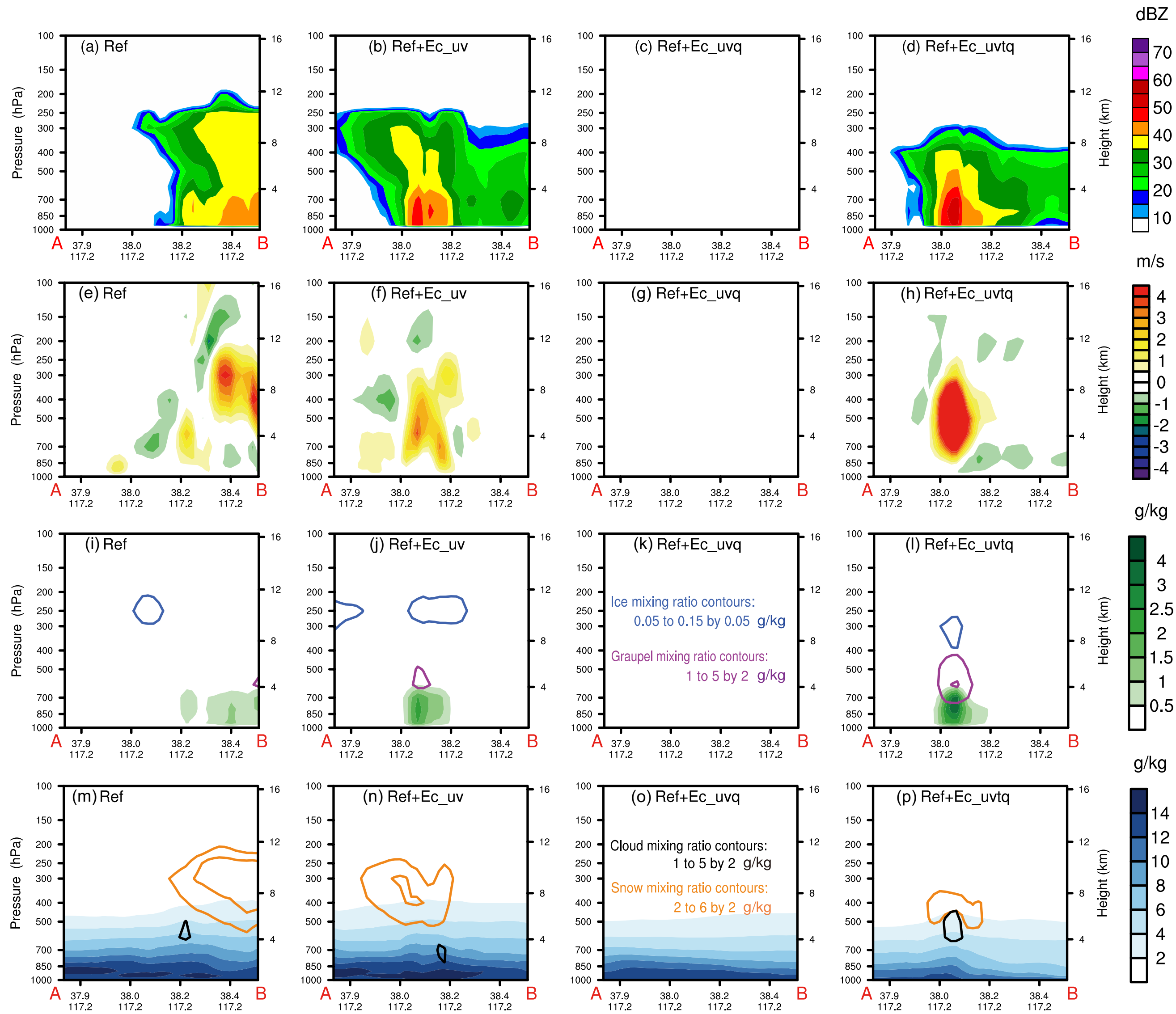

Fig. 10 Cross-sections of the radar reflectivity (**a**–**d**), vertical velocity (**e**–**h**), rainwater mixing ratio (filled colors, **i**–**l**), and water vapor mixing ratio (filled colors, **m**–**p**) along line A–B in Fig. 9e for the Ref (**a**, **e**, **i**, **m**), Ref+Ec_uv (**b**, **f**, **j**, **n**), Ref+Ec_uvq (**c**, **g**, **k**, **o**), and Ref+Ec_uvtq (**d**, **h**, **l**, **p**) experiments for the North case at 1900 UTC on 4 July 2020. The contours in **i**–**l** are for ice and graupel mixing ratios, and those in **m**–**p** are for cloud water and snow mixing ratios

Specifically, the u, v, and T fields are nudged during the simulation periods before and after the high-frequency cyclical assimilation of radar reflectivity observations, while the q field is only nudged during the simulation period after the high-frequency cyclical assimilation of radar reflectivity observations.

Two heavy rainfall events under different water vapor background conditions are selected for the test. The results show that the experiment in which radar reflectivity data are cyclically assimilated with an interval of 20 min always produces overestimated and spurious precipitation for both cases. With the u, v fields nudged, the model always generates the best 6-h forecast for both cases, that is, the predicted strong echo positions can be effectively improved, and the false echo (and precipitation) predictions can be effectively suppressed. Although the forecast precipitation declined too quickly, nudging the q together with u, v fields produces a better forecast than the u, v fields alone in the first 3-h forecast for the South case, which occurs in the East Asian summer monsoon-affected area. However, for the North case, which occurs in the East Asian summer monsoon transition zone, nudging the q together with the u, v fields experiment yields unreliable rapid decay of echoes and precipitation forecasts. However, the precipitation forecast

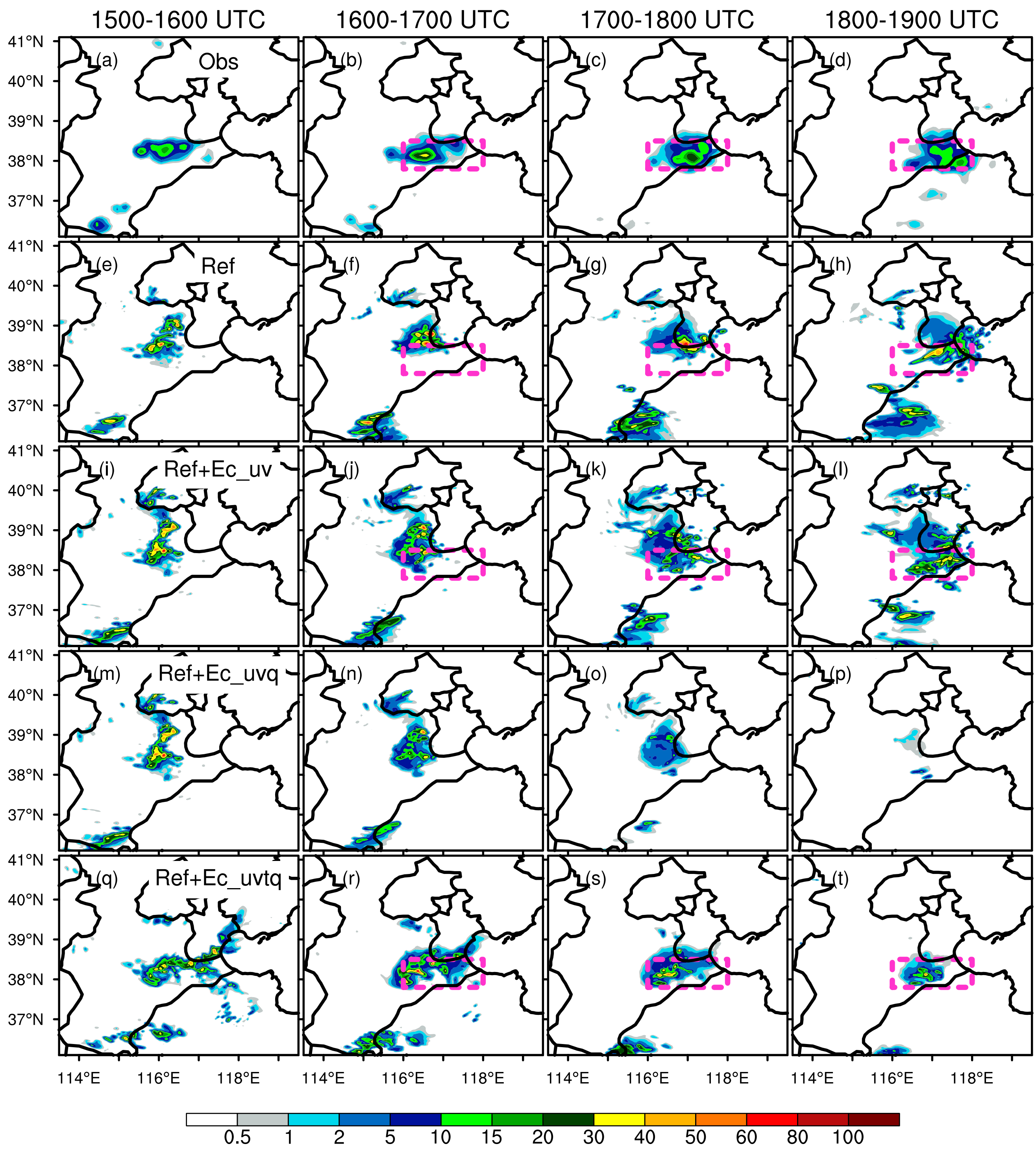

Fig. 11 Hourly accumulated precipitation (units: mm) for the North case on 4 July 2020 from **a–d** observations (Obs), the **e–h** Ref, **i–l** Ref+Ec_uv, **m–p** Ref+Ec_uvq, and **q–t** Ref+Ec_uvtq experiments. The last analysis time of the case is 1500 UTC on 4 July 2020. The areas framed by the dotted purple lines in **b–d**, **f–h**, **j–l**, and **r–t** indicate the observed main rain zone

can be improved (with an increased chance of rainfall) by further nudging the T field (lower value than that of the Ref experiment) of the ECMWF global forecast data.

Our study finds that nudging the horizontal wind field of the ECMWF global forecast data before and after radar reflectivity data are cyclically assimilated at high-frequencies would be beneficial for position correction of

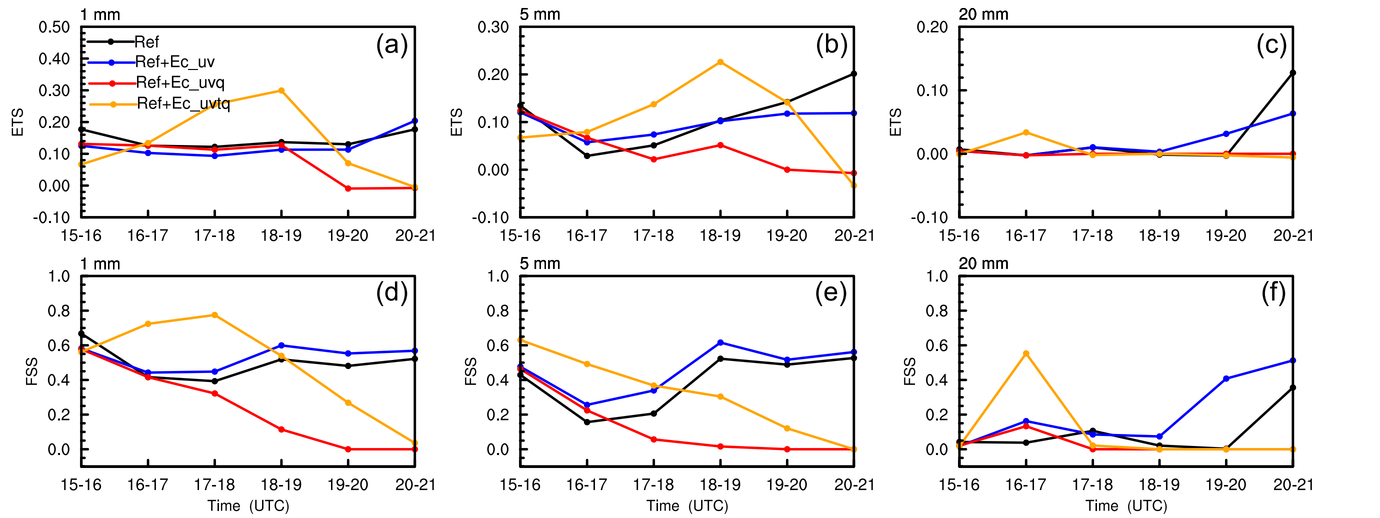

Fig. 12 ETS (**a–c**) and FSS (**d–e**) of the predicted hourly accumulated precipitation of the Ref, Ref+Ec_uv, Ref+Ec_uvq, and Ref+Ec_uvtq experiments for thresholds of 1, 5, and 20 mm/h for the North case on 4 July 2020

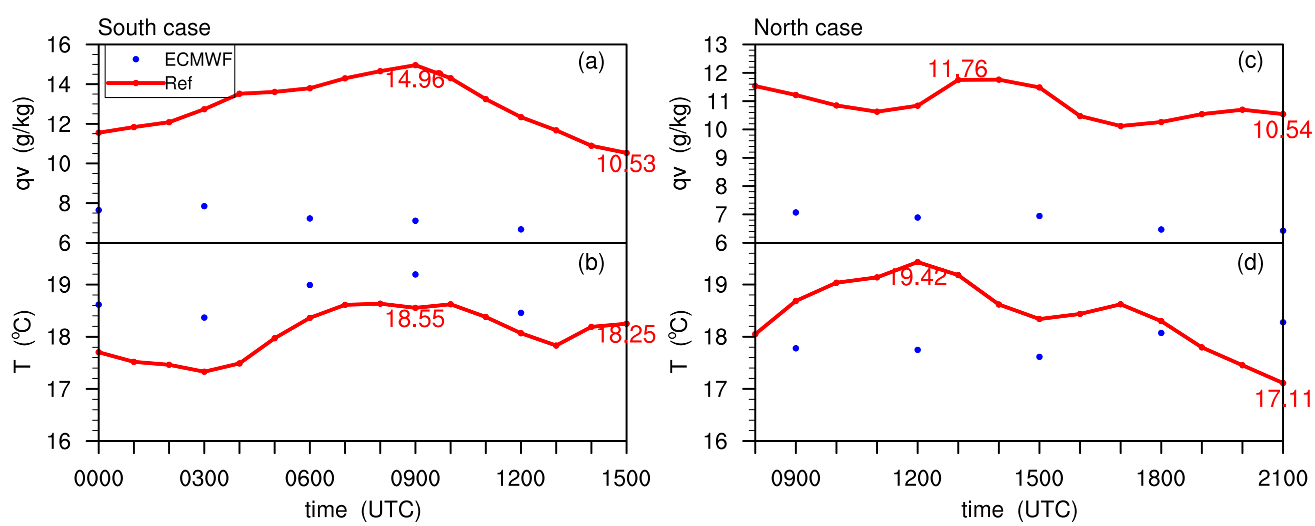

Fig. 13 The area-averaged water vapor mixing ratio (**a**) and temperature (**b**) at 850 hPa from the ECMWF global forecast data (ECMWF) and the Ref experiment (Ref) for the South case on 6 July 2019. **c**, **d** Are the same as **a** and **b** but are for the North case on 4 July 2020. The area (32°–34.5° N, 118°–120° E) for the South case and the area (38°–39° N, 115°–116° E) for the North case are used for averaging

precipitation forecasting. The effect of further nudging the water vapor mixing ratio or temperature is uncertain and is strongly dependent on the environmental condition field that leads to precipitation and the bias between the large-scale analysis and the model. However, we believe that the spatial pattern of the humidity field offered by the ECMWF global forecast data is valuable for constraining the overwetted analysis field after multiple assimilations of radar reflectivity data. In this study, a nudging coefficient of 9×10^{-4} (s^{-1}) is used, and perhaps weaker constraints with smaller nudging coefficients will produce better results; this requires more experiments for verification. In addition, the large-scale constraints are imposed on the model during the periods before or after analysis times in this study, and the effect of large-scale constraints imposed on analysis times or imposed on separate periods (before or after analysis times) needs further discussion.

Acknowledgments This work was supported by the Key Laboratory of Climate Resource Development and Disaster Prevention of Gansu Province (ACRE-2021-XM01), the National Natural Science Foundation of China (41975111), the Youth Science and Technology Foundation Program of Gansu Province (20JR5RA112) and the Supercomputing Center of Lanzhou University. The authors thank the Chinese Meteorological Administration for providing the ECMWF global forecast data, radar observations, and precipitation observation data. We also thank the NCEP for providing the GFS data and the ECMWF for providing the ERA5 data.

Author contributions YY developed the idea for the study. HL and YY did the analysis and wrote the first draft of the manuscript. All authors contributed to the revisions and approved the final manuscript.

Funding This work was supported by the Key Laboratory of Climate Resource Development and Disaster Prevention of Gansu Province (ACRE-2021-XM01), the National Natural Science Foundation of China (41975111), and the Youth Science and Technology Foundation Program of Gansu Province (20JR5RA112).

Availability of data The ECMWF global forecast, radar, and precipitation data are provided by the Chinese Meteorological Administration, and can be obtained via request from http://www.cma.gov.cn/en2014/. The NCEP GFS data (https://rda.ucar.edu/datasets/ds084.1/) and ERA5 data (https://cds.climate.copernicus.eu/cdsapp#!/dataset/reanalysis-era5-pressure-levels?tab=form) used in this study are available for download at the websites.

Declarations

Conflict of interest The authors declare no conflict of interests or competing financial interests.

References

Aksoy A, Dowell DC, Snyder C (2009) A multicase comparative assessment of the ensemble Kalman filter for assimilation of radar observations. Part I: storm-scale analyses. Mon Weather Rev 137:1805–1824. https://doi.org/10.1175/2008MWR2691.1

Aksoy A, Dowell DC, Snyder C (2010) A multicase comparative assessment of the ensemble Kalman filter for assimilation of radar observations. Part II: short-range ensemble forecasts. Mon Weather Rev 138:1273–1292. https://doi.org/10.1175/2009MWR3086.1

Albers SC, McGinley JA, Birkenheuer DA, Smart JR (1996) The local analysis and prediction system (LAPS): analysis of clouds, precipitation and temperature. Wea Forecasting 11:273–287. https://doi.org/10.1175/1520-0434(1996)011%3c0273:TLAAPS%3e2.0.CO;2

Bannister RN, Chipilski HG, Martinez-Alvarado O (2020) Techniques and challenges in the assimilation of atmospheric water observations for numerical weather prediction towards convective scales. Q J R Meteorol Soc 146(726):1–48. https://doi.org/10.1002/qj.3652

Chou M-D, Suarez MJ (1999) A solar radiation parameterization (CLIRAD-SW) for atmospheric studies. NASA Technical Reports Series on Global Modeling and Data Assimilation, p 15

Clark P, Roberts N, Lean H, Ballard SP, Charlton-Perez C (2016) Convection-permitting models: a step-change in rainfall forecasting. Meteorol Appl 23(2):165–181. https://doi.org/10.1002/met.1538

Dong JL, Xue M (2013) Assimilation of radial velocity and reflectivity data from coastal WSR-88D radars using an ensemble Kalman filter for the analysis and forecast of landfalling hurricane Ike (2008). Q J R Meteorol Soc 139:467–487. https://doi.org/10.1002/qj.1970

Dowell DC, Wicker LJ, Snyder C (2011) Ensemble Kalman filter assimilation of radar observations of the 8 May 2003 Oklahoma City supercell: influences of reflectivity observations on storm-scale analyses. Mon Weather Rev 139:272–294. https://doi.org/10.1175/2010MWR3438.1

Gan R, Yang Y, Qiu X, Liu P, Wang X, Gu K (2022) A scheme to suppress spurious convection by assimilating the "zero" column maximum vertical velocity. J Geophys Res Atmos 127:e2021JD035536. https://doi.org/10.1029/2021JD03553

Gandin LS, Murphy AH (1992) Equitable skill scores for categorical forecasts. Mon Weather Rev 120:361–370. https://doi.org/10.1175/1520-0493(1992)120%3c0361:ESSFCF%3e2.0.CO;2

Gao JD, Xue M, Shapiro A, Droegemeier K (1999) A variational method for the analysis of three-dimensional wind fields from two Doppler radars. Mon Weather Rev 127:2128–2142. https://doi.org/10.1175/1520-0493(1999)127%3c2128:AVMFTA%3e2.0.CO;2

Gao JD, Xue M, Brewster K, Droegemeier KK (2004) A three dimensional data analysis method with recursive filter for Doppler radars. J Atmos Oceanic Technol 21:457–469. https://doi.org/10.1175/1520-0426(2004)021,0457:ATVDAM.2.0.CO;2

Gao S, Sun J, Min J, Zhang Y, Ying Z (2018) A scheme to assimilate "no rain" observations from Doppler radar. Wea Forecasting 33:71–88. https://doi.org/10.1175/WAF-D-17-0108.1

Gong W, Shi C, Zhang T, Jiang L, Zhuang Y, Meng X (2015) Evaluation of surface meteorological elements from several numerical models in China (in Chinese). Clim Environ Res 20:53–62. https://doi.org/10.3878/j.issn.1006-9585.2014.13153

Hong S-Y, Lim J-OJ (2006) The WRF single-moment 6-class microphysics scheme (WSM6). J Korean Meteorol Sci 42:129–151

Hong S-Y, Noh Y, Dudhia J (2006) A new vertical diffusion package with an explicit treatment of entrainment processes. Mon Weather Rev 134:2318–2341. https://doi.org/10.1175/MWR3199.1

Hu M, Xue M (2007) Impact of configurations of rapid intermittent assimilation of WSR-88D radar data for the 8 May 2003 Oklahoma City tornadic thunderstorm case. Mon Weather Rev 135:507–525. https://doi.org/10.1175/MWR3313.1

Hu M, Xue M, Brewster K (2006a) 3DVAR and cloud analysis with WSR-88D Level-II data for the prediction of the Fort Worth tornadic thunderstorms. Part I: cloud analysis and its impact. Mon Weather Rev 134:675–698. https://doi.org/10.1175/MWR3092.1

Hu M, Xue M, Gao JD, Brewster K (2006b) 3DVAR and cloud analysis with WSR-88D Level-II data for the prediction of the Fort Worth tornadic thunderstorms. Part II: impact of radial velocity analysis via 3DVAR. Mon Weather Rev 134:699–721. https://doi.org/10.1175/MWR3093.1

Hu J, Gao J, Wang Y, Pan S, Fierro AO, Skinner PS, Knopfmeier K, Mansell ER, Heinselman PL (2021) Evaluation of an experimental Warn-on-Forecast 3DVAR analysis and forecast system on quasi-real-time short-term forecasts of high-impact weather events. Q J R Meteorol Soc 147:4063–4082. https://doi.org/10.1002/qj.4168

Jones CD, MacPherson B (1997) A latent heat nudging scheme for the assimilation of precipitation data into an operational mesoscale model. Meteorol Appl 4:269–277. https://doi.org/10.1017/s1350482797000522

Lai A, Gao J, Koch SE, Wang Y, Pan S, Fierro AO, Cui C, Min J (2019) Assimilation of radar radial velocity, reflectivity, and pseudowater vapor for convective-scale NWP in a variational framework. Mon Weather Rev 147:2877–2900. https://doi.org/10.1175/MWR-D-18-0403.1

Li Y, Wang X, Xue M (2012) Assimilation of radar radial velocity data with the WRF hybrid ensemble-3DVAR system for the prediction of Hurricane Ike (2008). Mon Weather Rev 140:3507–3524. https://doi.org/10.1175/MWR-D-12-00043.1

Lin E, Yang Y, Qiu X, Xie Q, Gan R, Zhang B, Liu X (2021) Impacts of the radar data assimilation frequency and large-scale constraint on the short-term precipitation forecast of a severe convection case. Atmos Res 257:105590. https://doi.org/10.1016/j.atmosres.2021.105590

Liu Y, Zhang T, Duan H, Wu J, Zeng D, Zhao C (2021) Evaluation of forecast performance for four meteorological models in summer

over Northwestern China. Front Earth Sci. https://doi.org/10.3389/feart.2021.771207
Maiello I, Ferretti R, Gentile S, Montopoli M, Picciotti E, Marzano FS, Faccani C (2014) Impact of radar data assimilation for the simulation of a heavy rainfall case in central Italy using WRF-3DVAR. Atmos Meas Tech 7:2919–2935. https://doi.org/10.5194/amt-7-2919-2014
Mandapaka PV, Germann U, Panziera L, Hering A (2012) Can Lagrangian extrapolation of radar fields be used for precipitation nowcasting over complex alpine orography? Wea Forecasting 27:28–49. https://doi.org/10.1175/WAF-D-11-00050.1
Mlawer EJ, Taubman SJ, Brown PD, Iacono MJ, Clough SA (1997) Radiative transfer for inhomogeneous atmospheres: RRTM, a validated correlated-k model for the longwave. J Geophys Res Atmos 102:16663–16682. https://doi.org/10.1029/97JD00237
Pan YJ, Wang MJ (2019) Impact of the assimilation frequency of radar data with the ARPS 3DVar and cloud analysis system on forecasts of a squall line in southern China. Adv Atmos Sci 36:160–172. https://doi.org/10.1007/s00376-018-8087-5
Ran Q, Fu W, Liu Y, Li T, Shi K, Sivakumar B (2018) Evaluation of quantitative precipitation predictions by ECMWF, CMA, and UKMO for flood forecasting: application to two basins in China. Nat Hazards Rev 19:05018003. https://doi.org/10.1061/(ASCE)NH.1527-6996.0000282
Roberts NM, Lean HW (2008) Scale-selective verification of rainfall accumulations from high-resolution forecasts of convective events. Mon Weather Rev 136:78–97. https://doi.org/10.1175/2007MWR2123.1
Schwartz CS, Liu Z (2014) Convection-permitting forecasts initialized with continuously cycling limited-area 3DVAR, ensemble Kalman filter, and '"hybrid"' variational–ensemble data assimilation systems. Mon Weather Rev 142:716–738. https://doi.org/10.1175/MWR-D-13-00100.1
Shen FF, Min JZ, Xu DM (2016) Assimilation of radar radial velocity data with the WRF Hybrid ETKF-3DVAR system for the prediction of Hurricane Ike (2008). Atmos Res 169:127–138. https://doi.org/10.1016/j.atmosres.2015.09.019
Snook N, Xue M, Jung Y (2015) Multiscale EnKF assimilation of radar and conventional observations and ensemble forecasting for a tornadic mesoscale convective system. Mon Weather Rev 143:1035–1057. https://doi.org/10.1175/MWR-D-13-00262.1
Snyder C, Zhang F (2003) Assimilation of simulated Doppler radar observations with an ensemble Kalman filter. Mon Weather Rev 131:1663–1677. https://doi.org/10.1175//2555.1
Sokol Z, Zacharov P (2012) Nowcasting of precipitation by an NWP model using assimilation of extrapolated radar reflectivity. Q J R Meteorol Soc 138:1072–1082. https://doi.org/10.1002/qj.970
Stauffer DR, Seaman NL (1990) Use of four-dimensional data assimilation in a limited-area mesoscale model. Part I: experiments with synoptic-scale data. Mon Weather Rev 118:1250–1277. https://doi.org/10.1175/1520-0493(1990)118%3c1250:UOFDDA%3e2.0.CO;2
Sun J, Crook NA (1997) Dynamical and microphysical retrieval from Doppler radar observations using a cloud model and its adjoint. Part I: model development and simulated data experiments. J Atmos Sci 54:1642–1661. https://doi.org/10.1175/1520-0469(1997)054%3c1642:DAMRFD%3e2.0.CO;2
Sun J, Crook NA (1998) Dynamical and microphysical retrieval from Doppler radar observations using a cloud model and its adjoint. Part II: retrieval experiments of an observed Florida convective storm. J Atmos Sci 55:835–852. https://doi.org/10.1175/1520-0469(1998)055%3c0835:DAMRFD%3e2.0.CO;2
Sun J et al (2014) Use of NWP for nowcasting convective precipitation: recent progress and challenges. Bull Am Meteorol Soc 95:409–426. https://doi.org/10.1175/BAMS-D-11-00263.1
Supinie TA, Yussouf N, Jung Y, Xue M, Cheng J, Wang S (2017) Comparison of the analyses and forecasts of a tornadic supercell storm from assimilating phased-array radar and WSR-88D observations. Wea Forecasting 32:1379–1401. https://doi.org/10.1175/waf-d-16-0159.1
Tang X, Chen B, Liang P, Qian W (2009) Defnition and features of the north edge of Asian summer monsoon (in Chinese). Acta Meteorol Sin 67:83–89. https://doi.org/10.3321/j.issn:0577-6619.2009.01.009
Tang X, Sun J, Zhang Y, Tong W (2019) Constraining the large-scale analysis of a regional rapid-update-cycle system for short-term convective precipitation forecasting. J Geophys Res Atmos 124:6949–6965. https://doi.org/10.1029/2018JD030190
Tong MJ, Xue M (2005) Ensemble Kalman filter assimilation of Doppler radar data with a compressible nonhydrostatic model: OSS experiments. Mon Weather Rev 133:1789–1807. https://doi.org/10.1175/MWR2898.1
Vendrasco EP, Sun J, Herdies DL, de Angelis CF (2016) Constraining a 3DVAR radar data assimilation system with large-scale analysis to improve short-range precipitation forecasts. J Appl Meteorol Climatol 55:673–690. https://doi.org/10.1175/JAMC-D-15-0010.1
Wang H, Sun J, Fan S, Huang X-Y (2013) Indirect assimilation of radar reflectivity with WRF 3D-Var and its impact on prediction of four summertime convective events. J Appl Meteorol Climatol 52:889–902. https://doi.org/10.1175/JAMC-D-12-0120.1
Wang R, Gong J, Wang H (2021) Impact studies of introducing a large-scale constraint into the kilometer-scale regional variational Data Assimilation (in Chinese). Chin J Atmos Sci 45:1007–1022. https://doi.org/10.3878/j.issn.1006-9895.2009.20176
Xiao Q, Zhang XY, Davis C, Tuttle J, Holland G, Fitzpatrick PJ (2009) Experiments of hurricane initialization with airborne Doppler radar data for the advanced research hurricane WRF (AHW) model. Mon Weather Rev 137:2758–2777. https://doi.org/10.1175/2009MWR2828.1
Yue X, Shao A, Fang X, Li L (2018) Incorporating a large-scale constraint into radar data assimilation to mitigate the effects of large-scale bias on the analysis and forecast of a squall line over the Yangtze-Huaihe river basin. J Geophys Res Atoms 123:8581–8598. https://doi.org/10.1029/2018JD028362
Zeng J, Zhang Q, Wang CL (2016) Spatial-temporal pattern of surface energy fluxes over monsoon edge area in China and its relationship with climate (in Chinese). Acta Meteorol Sin 74:876–888. https://doi.org/10.11676/qxxb2016.064
Zeng Y, Janjic T, de Lozar A, Welzbacher CA, Blahak U, Seifert A (2021) Assimilating radar radial wind and reflectivity data in an idealized setup of the COSMO-KENDA system. Atmos Res 249:105282. https://doi.org/10.1016/j.atmosres.2020.105282
Zhao K, Xue M (2009) Assimilation of coastal Doppler radar data with the ARPS 3DVAR and cloud analysis for the prediction of Hurricane Ike (2008). Geophys Res Lett 36:L12803. https://doi.org/10.1029/2009GL038658
Zhao K, Li X, Xue M, Jou BJ-D, Lee W-C (2012) Short-term forecasting through intermittent assimilation of data from Taiwan and mainland China coastal radars for Typhoon Meranti (2010) at landfall. J Geophys Res 117:D06108. https://doi.org/10.1029/2011JD017109

Publisher's Note Springer Nature remains neutral with regard to jurisdictional claims in published maps and institutional affiliations.